ACS OMEGA

Open Access

http://pubs.acs.org/journal/acsodf

Article

Engineering of $Cd_xZn_{1-x}S$ Nanomaterials for Fabrication of Hybrid $Cd_xZn_{1-x}S$/Si Heterojunction Broadband Photo Detectors

Priyanka Das,* Satyajit Saha,* and Amit Kumar Bhunia*

Cite This: *ACS Omega* 2025, 10, 294−305

Read Online

ACCESS | Metrics & More | Article Recommendations

ABSTRACT: Effective engineering of nanostructured materials provides a scope to explore the underlying photoelectric phenomenon completely. A simple cost-effective chemical reduction route is taken to grow nanoparticles of $Cd_xZn_{1-x}S$ with varying x = 1, 0.7, 0.5, 0.3, and 0. X-ray diffraction confirms the formation of different phases of targeted $Cd_xZn_{1-x}S$, while field emission scanning electron microscopy shows change of nanostructures. Energy-dispersive X-ray spectroscopy determines the composition of the grown nanostructures as CdS, $Cd_{0.7}Zn_{0.3}S$, $Cd_{0.5}Zn_{0.5}S$, $Cd_{0.3}Zn_{0.7}S$, and ZnS. The optical absorption study determines the band gap shift with change of composition as well as with quantum confinement. The fluorescence lifetime for each nanomaterial is determined by time-correlated single photon counting, and Raman analysis revealed that ZnS exhibits the highest blue shift. Thus, there is a possibility to apply such grown nanomaterials for fabrication of heterojunction-based photodetectors (PDs) in a broad wavelength region. $Cd_xZn_{1-x}S$ nanostructures on n-type bulk silicon (Si) were successfully fabricated by a simple cost-effective spin coating method and present hybrid heterojunction PDs. The fabricated p−n heterojunction exhibits good rectifying behavior at room temperature under a reverse bias condition. Also, it was observed that the heterojunction is extremely sensitive to the irradiation of visible light because of the significant optoelectric effect with a good I_{light}/I_{dark} ratio (here, I_{light} is the current in the presence of light and I_{dark} is the dark current), quick response time (40 to 1005 ms), and good reproducibility (three cycles of I_{light}/I_{dark} for each sample are observed). It was observed that the responsivity value gradually decreases for x = 1 to x = 0 in the $Cd_xZn_{1-x}S$/n-Si heterojunction, i.e., it is maximum for CdS NRs (6.74×10^{-3} mA/W), intermediate for $Cd_{0.5}Zn_{0.5}S$ NPs (4.49×10^{-3} mA/W), and minimum for ZnS NPs (2.72161×10^{-4} mA/W). A similar nature has been observed in the case of detectivity, and hence it is a maximum (1.45×10^{6} Jones) for CdS NRs. The photocurrent generation at the heterojunction showed excellent "on" and "off" switching behavior in the presence and absence of light illumination. Response time and gain change significantly with change of composition. The responsivity and detectivity with good photoresponse originated from the realization of special microstructures, enhancing the photoelectric behavior of $Cd_xZn_{1-x}S$ materials for applications in low-dimensional PDs covering a large wavelength region.

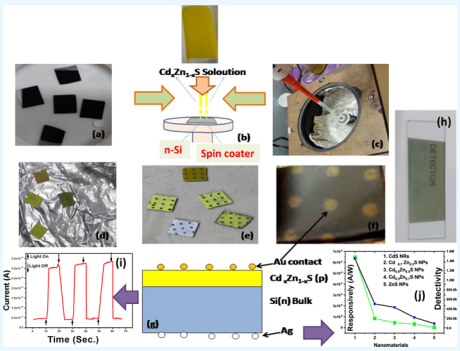

1. INTRODUCTION

Growing materials with the right nanostructures (nanowires, nanorods, nanosheets, nanoflowers, nanotubes, nanoparticles, etc.) in a controllable manner presents a challenge for the fabrication of various functional devices. It is also possible to develop additional functionalities that stem from reduced dimensionality.[1−6] The chemical route is a cost-effective way to fabricate the desired nanostructures for semiconductors.[7,8] Nanostructured semiconductors possessing photoconductivity are useful for photovoltaic applications and photodetection. Hence, in the present work, photoconductive $Cd_xZn_{1-x}S$ (varying x) nanomaterials are grown by the chemical reduction route. The grown nanomaterials are characterized structurally and optically. Nanostructures are an ideal choice to be a good photodetector (PD)[9−12] because it allows for shortening of the charge carrier lifetime due to very small absorption region and high surface area to volume ratio. Thus, $Cd_xZn_{1-x}S$ nanomaterials will be effective PDs in a wide region of wavelength. In photovoltaic applications, where the material has represented a wide gap window material in the visible and near-infrared areas, nanocrystalline cadmium sulfide (CdS) films placed over silicon have also attracted a lot of interest.[13] ZnS is a very good and useful material for optoelectronics applications.[13] According to Tapan and Afrailov, photons with wavelengths between 340 and 800 nm have a very high quantum efficiency in a heterojunction photodiode device made of zinc sulfide and silicon (ZnS−Si).[14] According to Liu and Yue, the surface of silicon nanopillars with a ZnS layer is beneficial for photoresistor applications.[15] The

Received: June 28, 2024
Revised: December 3, 2024
Accepted: December 3, 2024
Published: December 26, 2024

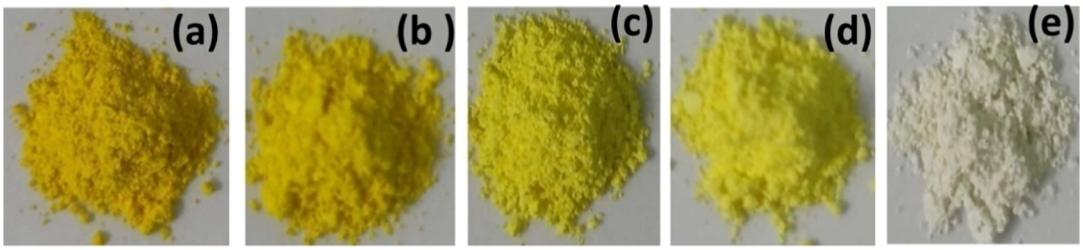

Figure 1. Color of the different powder sample: (a) CdS NRs, (b) $Cd_{0.7}Zn_{0.3}S$ NPs, (c) $Cd_{0.5}Zn_{0.5}S$ NPs, (d) $Cd_{0.3}Zn_{0.7}S$ NPs, and (e) ZnS NPs.

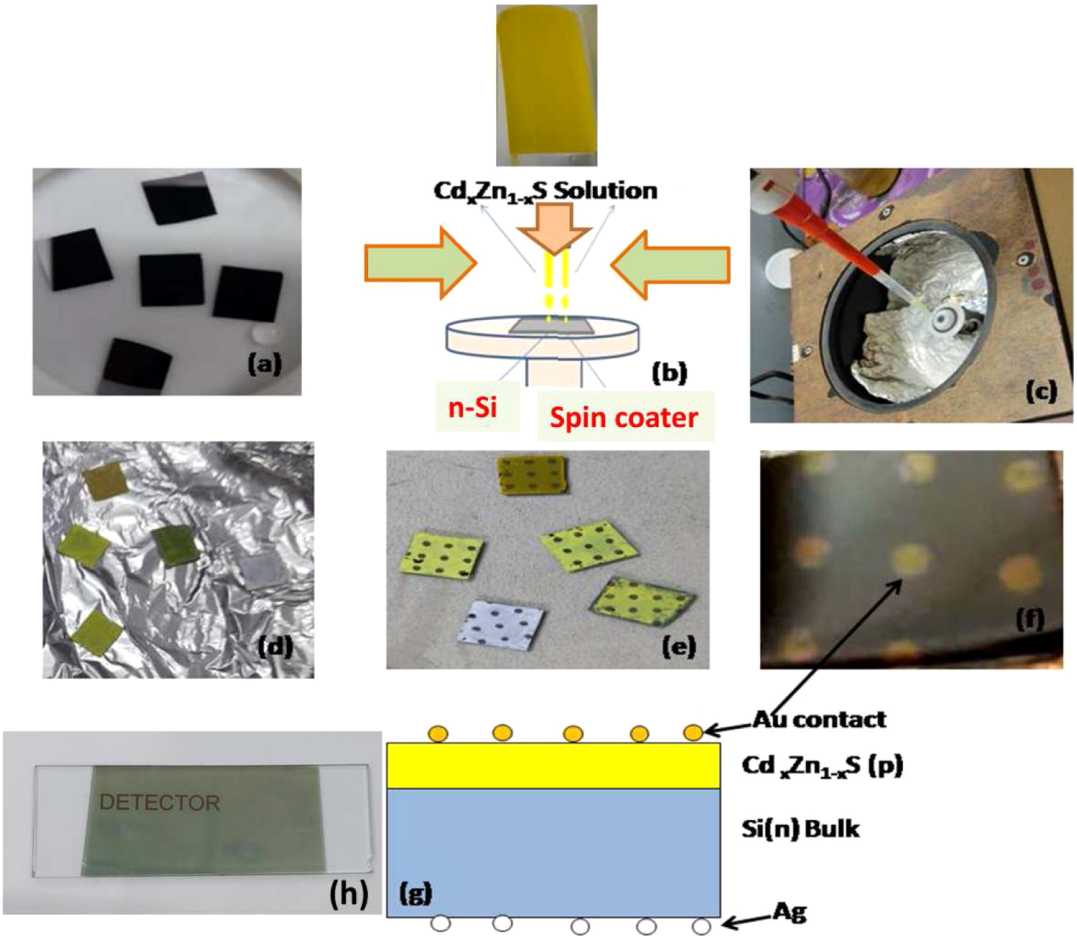

Figure 2. Schematic of the different steps for the fabrication of heterojunction device of $Cd_xZn_{1-x}S$ (p)/Si(n): (a) etched Si wafers, (b) schematic spin coating arrangement, (c) drop cast of $Cd_xZn_{1-x}S$ on Si wafers, (d) wafers after spin coating of $Cd_xZn_{1-x}S$, (e) spin-coated $Cd_xZn_{1-x}S$ wafers after gold contact, (f) top view of gold contact on wafer, (g) heterojunction device configuration of $Cd_xZn_{1-x}S$ (p)/Si(n), and (h) transparency of Au film.

bulk ZnS is less stable in the environment due to the higher probability of the oxide formation state. Band gap variation and variations of the optoelectronic properties are not possible in bulk. So, the need for ZnS nanoparticles is very urgent because it is comparatively highly stable. Nanoscale ZnS showed tuning of band gap with tuning size, morphology, and doping with metals. ZnS NPs responses are in visible light, though its band gap tuning on the nanoscale is large and close to the UV region; it detects the possibility of a lower edge of the visible region due to the presence of a defect state nanoscale and other important nanoscale properties.

PDs are being employed extensively in a wide range of applications, including fame detection, communications, surveillance, and environmental monitoring.[16−22] A device that can transform an optical signal at the input into an electrical signal at the output is known as a PD.[20] Fundamentally, the operation of a PD relies on the rate at which excitons, or electron−hole pairs, are generated in semiconductors when exposed to light energy above the material bandgap and on the effective movement and accumulation of the photogenerated carriers when subjected to an internal or external electric field, which generates photocurrent.[20] One of the main factors used to choose commercial applications is the PDs' performance and responsivity.

The choice of materials affects the device efficiency, photocurrent responsiveness, and operating wavelength. Due to their intriguing optical and electrical characteristics, heterojunctions are a popular choice for use in solar cells and other optoelectronic devices.

https://doi.org/10.1021/acsomega.4c06008
ACS Omega 2025, 10, 294−305

In this work semiconductor nanostructure $Cd_xZn_{1-x}S$ (for the x = 1, 0.7, 0.5, 0.3, and 0)/n-Si form hybrid heterojunctions, and these are preferred as PDs. The change in composition with change of "x" leads to change of band gap. The performance of the devices as PDs with change of composition are studied and the properties like responsivity, detectivity, response time, and gain are compared. Thus, the objective of the work is to present the optoelectronic properties of the fabricated PDs based on different grown compositions in $Cd_xZn_{1-x}S$. The change of composition means that PDs will be effective in a wide range of wavelength region. Our aim is to grow good PDs out of these grown heterojunctions, which can be useful in communication technology and in various sensors for safety monitoring.[23−28]

2. EXPERIMENT

2.1. Process of Synthesizing Nanoparticles through the Chemical Reduction Route. Here, we fabricated nanomaterials CdS, $Cd_xZn_{1-x}S$ (for the x = 1, 0.7, 0.5, 0.3, and 0), and ZnS using an easy and affordable chemical precipitation approach.[8] In order to make CdS, $Cd_{0.7}Zn_{0.3}S$, $Cd_{0.5}Zn_{0.5}S$, $Cd_{0.3}Zn_{0.7}S$, and ZnS, the initial ingredients' proportions of $CdCl_2$ and $ZnCl_2$ had to be varied. We introduced THF, as a capping agent, and a stoichiometric amount of $CdCl_2$ into a beaker. The mixture is stirred using a magnetic stirrer. After stirring for a few minutes, the stochiometric amount of sulfur powder is added and finally the reducing agent $NaBH_4$ is added to the solution, which is stirred for 16 h. The precipitate is centrifuged as well as washed with DI water, and finally the sample is dried. ZnS nanoparticles are synthesized using a similar procedure, with $ZnCl_2$ serving as the precursor.[8] Using stoichiometric amounts of $CdCl_2$ and $ZnCl_2$ powders according to the molar ratios of the desired chemical, such as $Cd_{0.7}Zn_{0.3}S$, $Cd_{0.5}Zn_{0.5}S$, and $Cd_{0.3}Zn_{0.7}S$, $Cd_xZn_{1-x}S$ is synthesized. $ZnCl_2$ serves as the precursor in a similar procedure used to grow ZnS nanoparticles.[8] Stoichiometric amounts of $CdCl_2$ and $ZnCl_2$ powders are used in the synthesis of $Cd_xZn_{1-x}S$ in accordance with the molar ratios of the target product, such as $Cd_{0.7}Zn_{0.3}S$, $Cd_{0.5}Zn_{0.5}S$, and $Cd_{0.3}Zn_{0.7}S$. The compositions of grown nanomaterial's are determined through energy-dispersive X-ray spectroscopy (EDAX) analysis and observed to be $Cd_{0.7}Zn_{0.3}S$, $Cd_{0.5}Zn_{0.5}S$, and $Cd_{0.3}Zn_{0.7}S$. Typical chemical reaction concerning the formation CdS from $CdCl_2$ and sulfur is shown below[8]

$$CdCl_2 \leftrightarrow Cd^{2+} + 2Cl^- \quad (1)$$

$$2NaBH_4 + 2Cl^- \rightarrow 2NaCl + B_2H_6 + 2H + 2e^- \quad (2)$$

$$2H + S \rightarrow H_2S \quad (3)$$

$$H_2S + Cd^{2+} + 2e^- \rightarrow CdS + H_2 \quad (4)$$

The changes of color with change of composition in $Cd_xZn_{1-x}S$ are shown in Figure 1. Increases in Zn content cause the precipitate to transition from yellowish to white. The nice color changes in the powder samples may be due to the nanoscale confined effect.

2.2. Fabrication of Heterojunctions. Having thoroughly characterized $Cd_xZn_{1-x}S$ nanostructures, PDs were fabricated with these nanomaterials grown on n-Si.[29] Silver (Ag) served as the back contact, and approximately 20 nm-thick gold (Au) islands were placed on top to guarantee that the Au electrode only absorbed a small portion of the light.[30] The layered structure consisted of Ag/n-Si/$Cd_xZn_{1-x}S$/Au. Figure 2 displays the schematic diagram used in the device construction.

Using ultrasonification, a 1 × 1 cm^2 n-Si(111) substrate was first cleaned with acetone, ethanol, and DI water multiple times.[30] The silicon wafer is then etched with HF and water in the ratio of 1:6 for 30 s. The etched silicon wafer is then thoroughly washed in DI water and dried. The nanoparticles (50 mg of $Cd_xZn_{1-x}S$ NPs) are dispersed in ethanol and ultrasonicated for 45 min. Next, the dispersed solution was spin coated for 30 s at 1500 rpm on an n-type Si wafer (Figure 2). The n-Si substrate coated with $Cd_xZn_{1-x}S$ NPs was annealed for 45 min at 50 °C. The same process was repeated for 5 samples taking the same amount of sample in ethanol for each case (Figure 2). The $Cd_xZn_{1-x}S$ NP thin film was then annealed for 45 min at 70 °C in a N_2 environment. The PD's active area is approximately 80 mm^2. The up contact has been done with "Au" by thermal evaporation. The gold metal contacts are of 1 mm diameter, and the back contact is done with "Ag" metal by thermal evaporation again. The schematic of the different steps of the device fabrication and device structure is shown in Figure 2.

2.3. Instrumentation for Device Characterization. The properties of the devices are characterized using an electrical probe station using the Keithley Semiconductor parameter analyzer [4200 SCS] and a broad band solar simulator. Current (I)−voltage (V) characteristics are observed under reverse bias in dark conditions and in the presence of visible light. The current (I)−time (t) curve is computed using magnified single pulse to determine response time at the −2 V bias condition. For visible light irradiation, a 500 W lamp is employed as the light source.

3. RESULTS AND DISCUSSION

3.1. Material Characterization. *3.1.1. X-ray Diffraction.* The grown nanomaterials are identified through the X-ray diffraction (XRD) pattern (Figure 3). The XRD spectrum of CdS NRs shows the presence of the (100), (002), (101), (102), (110), (103), and (112) diffraction peaks corresponding to the hexagonal wurzite crystal phase for CdS (JCPDS card no. 41-1049). This structure gradually changes toward the cubic phase with an increase of Zn content in $Cd_xZn_{1-x}S$ and finally becomes the cubic zinc blende phase in ZnS. The presence of (111), (220), and (311) diffraction peaks represents the cubic zinc blende phase of ZnS (JCPDS card no. 77-2100).

Average crystal size (P) is considered using the Scherrer equation[8,31]

$$P = k\lambda/\beta_{1/2}\cos\theta \quad (5)$$

where $\beta_{1/2}$ is the width at half of the maximum intensity, 2θ is the Bragg angle, and λ (for Cu Kα, λ = 1.5418 Å) is the X-ray wavelength. The crystal size is computed from the peak at 2θ around 25° for each composition. The crystal sizes vary between 10 nm for CdS and 5 nm for ZnS. Thus, the crystal size is reduced as the value of x decreases in $Cd_xZn_{1-x}S$. The crystal strain for all nanoparticles is calculated from the relation

$$\text{strain } (\varepsilon) = \frac{\beta_{1/2}}{4\tan\theta} \quad (6)$$

The calculated average strains for CdS NRs, $Cd_{0.7}Zn_{0.3}S$ NPs, $Cd_{0.5}Zn_{0.5}S$ NPs, $Cd_{0.3}Zn_{0.7}S$ NPs, and ZnS NPs nanoparticles are 0.015, 0.021, 0.025, 0.032, and 0.067, respectively. Hence,

https://doi.org/10.1021/acsomega.4c06008
ACS Omega 2025, 10, 294−305

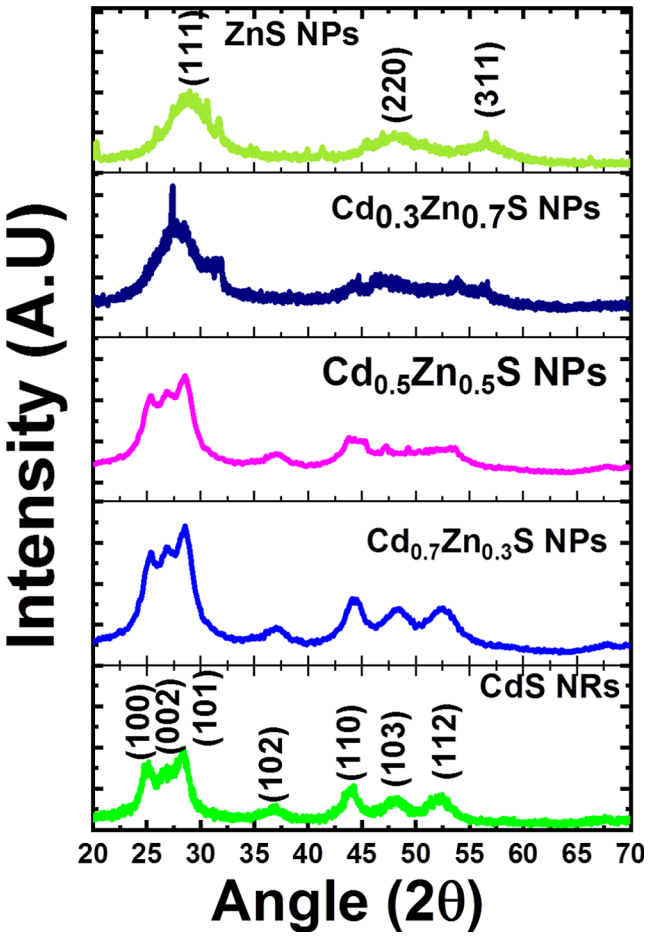

Figure 3. XRD pattern CdS NRs, $Cd_{0.7}Zn_{0.3}S$ NPs, $Cd_{0.5}Zn_{0.5}S$ NPs, $Cd_{0.3}Zn_{0.7}S$ NPs, and ZnS NPs.

strain gradually increases with the Zn content (0, 0.3, 0.5, 0.7, and 1) within $Cd_xZn_{1-x}S$ and maximum in ZnS NPs.

3.1.2. Field Emission Scanning Electron Microscopy Images. An electron source known as a field-emission gun is used in field emission scanning electron microscopy (FESEM) to provide an enhanced spatial resolution image of the nanostructures. The produced semiconductor nanomaterials, as shown by the FESEM images, are displayed in Figure 4. FFESEM pictures demonstrate rod-shaped nanoparticle production for CdS. However, as the Zn content rises, a portion of the rod-shaped structure gradually changes to a spherical structure; this is shown in the $Cd_{0.7}Zn_{0.3}S$ and $Cd_{0.5}Zn_{0.5}S$ samples. In the end, spherical-shaped nanoparticles are seen in the ZnS and $Cd_{0.3}Zn_{0.7}S$ samples.

3.1.3. EDAX Measurement. The purity of the materials and the atomic proportion of the elements in the produced nanoparticles are disclosed by energy dispersive analysis by X-ray (EDAX). The target composition is nearly reached through the chemical reduction process, according to the EDAX spectra, and the percentage of elements for each of the three compositions is displayed in Figure 5a–c. As intended, EDAX shows strong stoichiometries in $Cd_{0.7}Zn_{0.3}S$ and $Cd_{0.5}Zn_{0.5}S$, and $Cd_{0.3}Zn_{0.7}S$.

3.1.4. Optical Absorption. Optical absorption of fabricated nanostructures dispersed in ethanol is measured using a Carry 5000 UV–vis–NIR spectrophotometer. Optical absorption coefficients are estimated for each nanostructure in the wavelength range of 200–900 nm. The peak position for three compositions like CdS NRs, $Cd_{0.5}Zn_{0.5}S$ NPs, and ZnS NPs is shown in Figure 5d–f. The absorption peak position shifts to a lower wavelength as the composition changes from CdS NRs to ZnS NPs in $Cd_xZn_{1-x}S$.

The direct band gap is measured using the below relation 2[8,31]

$$(\alpha h\nu)^2 = \text{constant}\ (h\nu - E_g) \tag{7}$$

where E_g is the direct band gap energy and α is the optical absorption coefficient. The band gap is displayed in Figure 6 and can be calculated using the $(\alpha h\nu)^2$ vs $h\nu$ plot.

The bandgap energy is found to be 2.79 2.87, 2.94, 3.4, and 3.95 eV and corresponds to CdS NRs, $Cd_{07}Zn_{0.3}S$ NPs, $Cd_{0.5}Zn_{0.5}S$ NPs, $Cd_{0.3}Zn_{0.7}S$ NPs, and ZnS NPs. From the parameters in Table 1, it is also evident that for each material, the

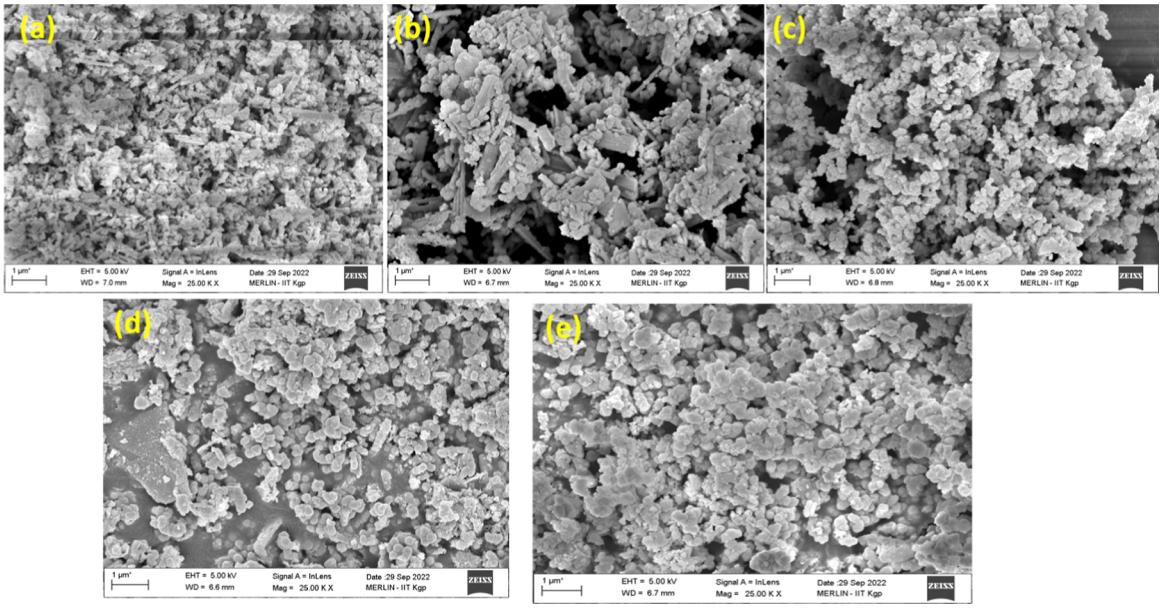

Figure 4. FESEM images of the (a) CdS NRs, (b) $Cd_{0.7}Zn_{0.3}S$ NPs, (c) $Cd_{0.5}Zn_{0.5}S$ NPs, (d) $Cd_{0.3}Zn_{0.7}S$ NPs, and (e) ZnS NPs.

https://doi.org/10.1021/acsomega.4c06008
ACS Omega 2025, 10, 294–305

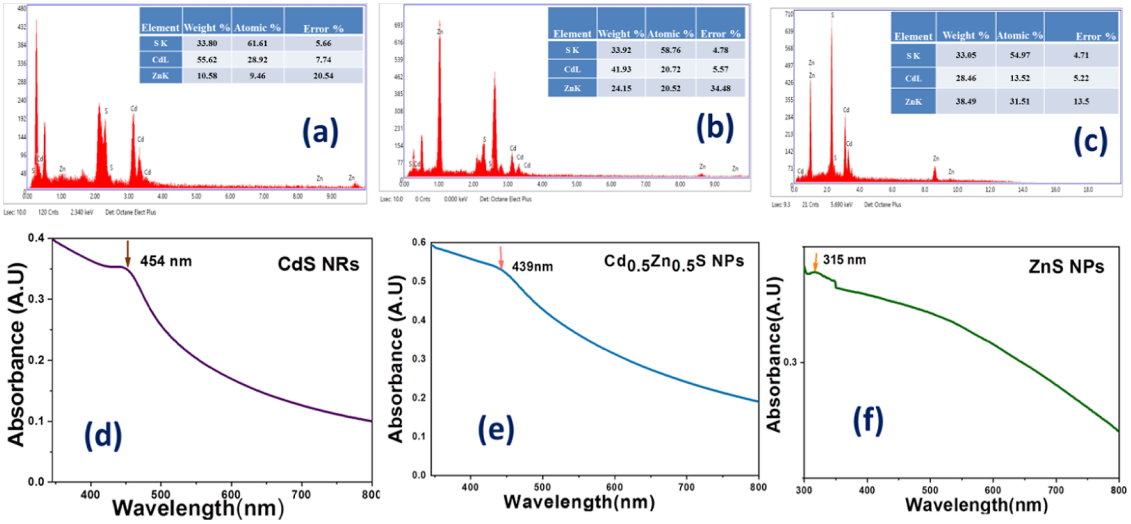

Figure 5. EDAX of (A) $Cd_{0.7}Zn_{0.3}S$ NRs plus NPs (B) $Cd_{0.5}Zn_{0.5}S$ NPs, (C) $Cd_{0.3}Zn_{0.7}S$ NPs, absorbance vs wavelength for (d) CdS NRs, (e) $Cd_{0.5}Zn_{0.5}S$ NPs, and (f) ZnS NPs.

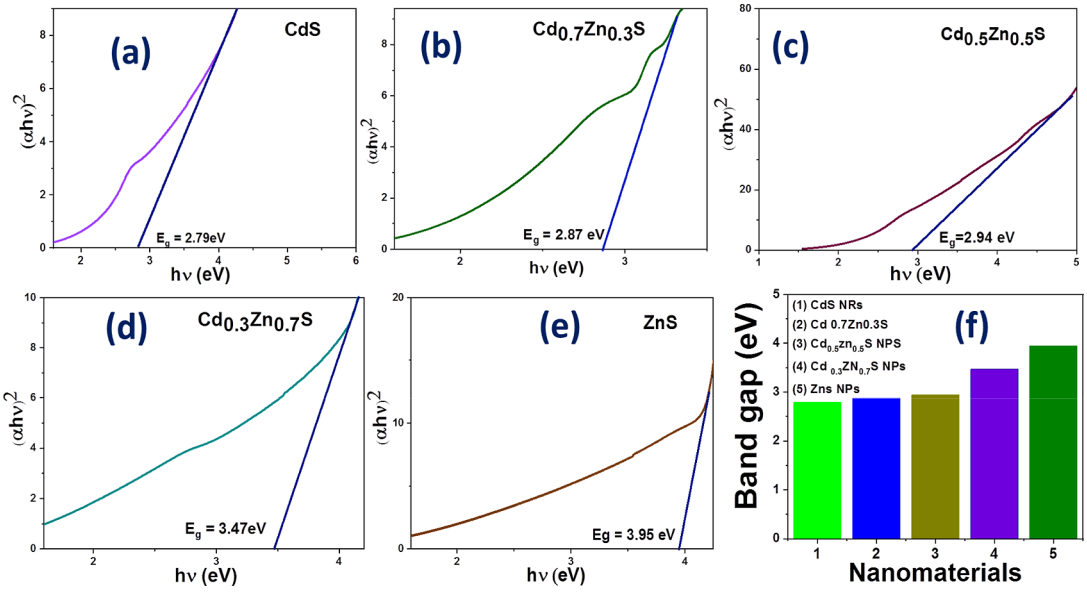

Figure 6. $(\alpha h\nu)^2$ vs hυ plot for $Cd_xZn_{1-x}S$ nanostructures with variation of x: (a) CdS NRs, (b) $Cd_{0.7}Zn_{0.3}S$ NPs, (c) $Cd_{0.5}Zn_{0.5}S$ NPs, (d) $Cd_{0.3}Zn_{0.7}S$ NPs, (e) ZnS NPs, and (f) histogram of bandgap for different nanomaterials.

Table 1. Comparison of Structural and Optical Parameters of $Cd_xZn_{1-x}S$ Nanostructures

grown sample	shape of nanostructures from FESEM	average crystal size (nm)	band gap energy (eV)	fluorescence lifetime (μs)	Raman shift cm^{-1}
CdS (hexagonal phase)	NRs	10	2.79	3.65	301.3
$Cd_{0.7}Zn_{0.3}S$	NRs and NPs	8.5	2.87	1.08	306
$Cd_{0.5}Zn_{0.5}S$	NPs	7.0	2.94	0.96	310
$Cd_{0.3}Zn_{0.7}S$ NPs	NPs	6.0	3.4	0.91	313
ZnS (cubic phase)	NPs	5.0	3.95	0.87	

band gap is large compared to their bulk values. A broad ranges of bandgap variation have been achieved for such semiconductor nanomaterials.

3.1.5. Raman Study. The Raman study provides Raman shift for each $Cd_xZn_{1-x}S$ with variation of x (Figure 7).

In comparison to bulk CdS, the Raman peak is red-shifted,[32] and the Raman peak for CdS nanorods at 301.3 cm^{-1} is associated with the first order longitudinal optical phonon mode.[33] However, blue shift occurs at 306, 310, and 313 cm^{-1} for the nanoparticles $Cd_{0.7}Zn_{0.3}S$, $Cd_{0.5}Zn_{0.5}S$, and $Cd_{0.3}Zn_{0.7}S$, respectively. An arrow (on different spectra) in Figure 7 indicates the relevant Raman peaks. However, the Raman peak for ZnS becomes insignificant compared to its own large fluorescence peak and hence does not appear within the wavenumber range 250 to 400 cm^{-1}.

3.1.6. Time-Correlated Single-Photon Counting Study. Time-correlated single-photon counting (TCSPC) is a method for quantifying fluorescence degradation in the temporal

https://doi.org/10.1021/acsomega.4c06008
ACS Omega 2025, 10, 294−305

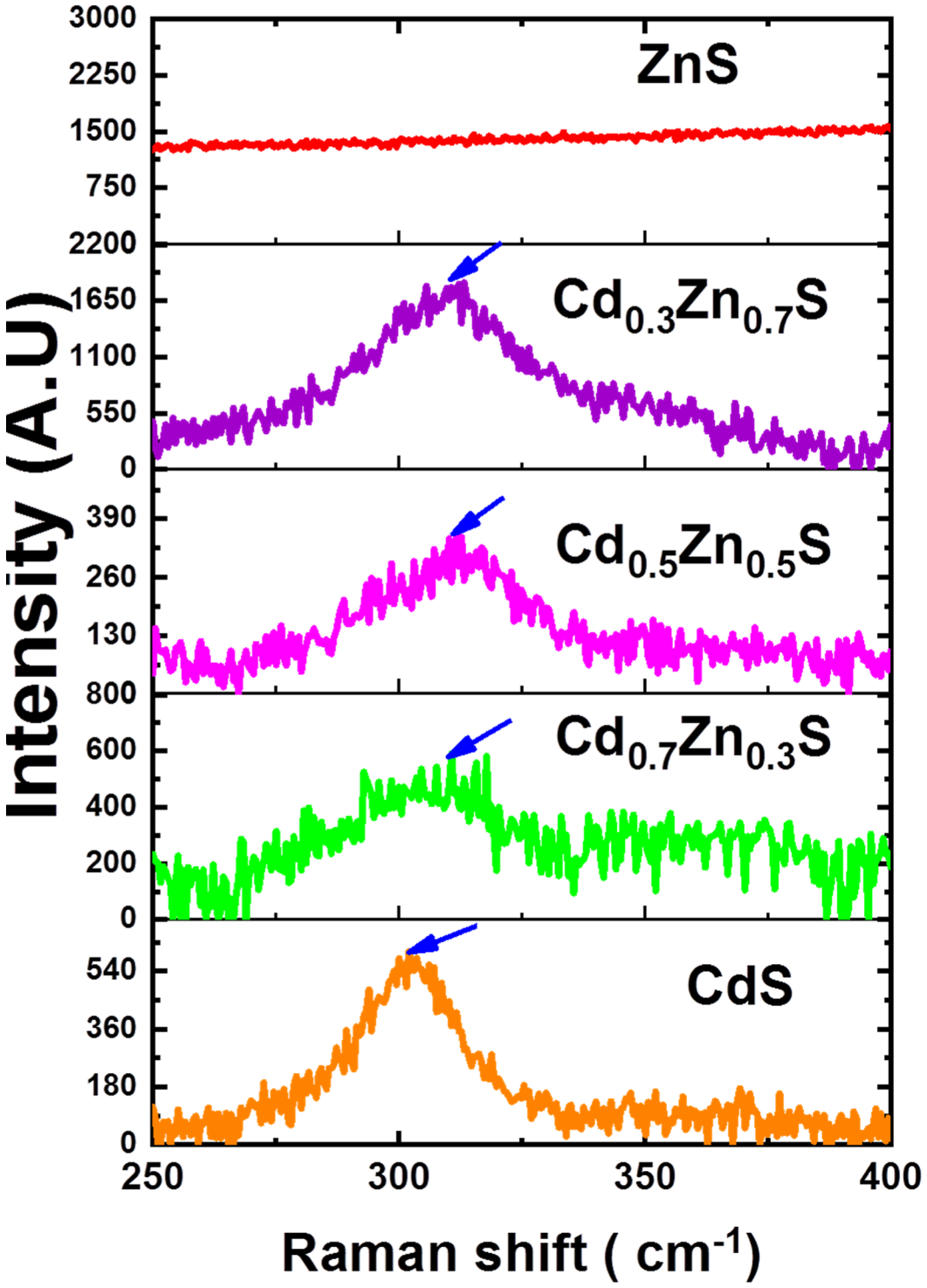

Figure 7. Raman shift for $Cd_xZn_{1-x}S$ nanostructures with variation of x.

domain. With this technique, single photon events are identified, and the laser pulse used to excite the sample is connected to the time of arrival of the photon events. For every composition, the decrease of fluorescence is monitored in the time domain (Figure 8). The lifetime for each nanomaterial is tabulated in Table 1. In $Cd_xZn_{1-x}S$, fluorescence lifetime diminishes as x decreases.

Thus, fluorescence lifetime is maximum ($\approx$3.65 μs) for CdS. However, as x decreases in $Cd_xZn_{1-x}S$, fluorescence lifetime decreases, and it is 0.87 μs for ZnS.

Growth of different nanostructures $Cd_xZn_{1-x}S$ is confirmed through XRD. The synthesis of $Cd_xZn_{1-x}S$ was done in the presence of capping agent tetrahydrofuran (THF). Hence, THF prevents the formation of larger crystallites and thus opposes Ostwald Ripening.[34,35] The XRD pattern indicates the transition from the hexagonal wurtzite phase for CdS to cubic zinc blende phase ZnS. Crystal size is obtained at fwhm corresponding to the same XRD peak (2θ) for each composition and is found to be 10 nm for CdS whereas 5 nm for ZnS. Hence, quantum confinement increases as x decreases in $Cd_xZn_{1-x}S$. FESEM

https://doi.org/10.1021/acsomega.4c06008
ACS Omega 2025, 10, 294−305

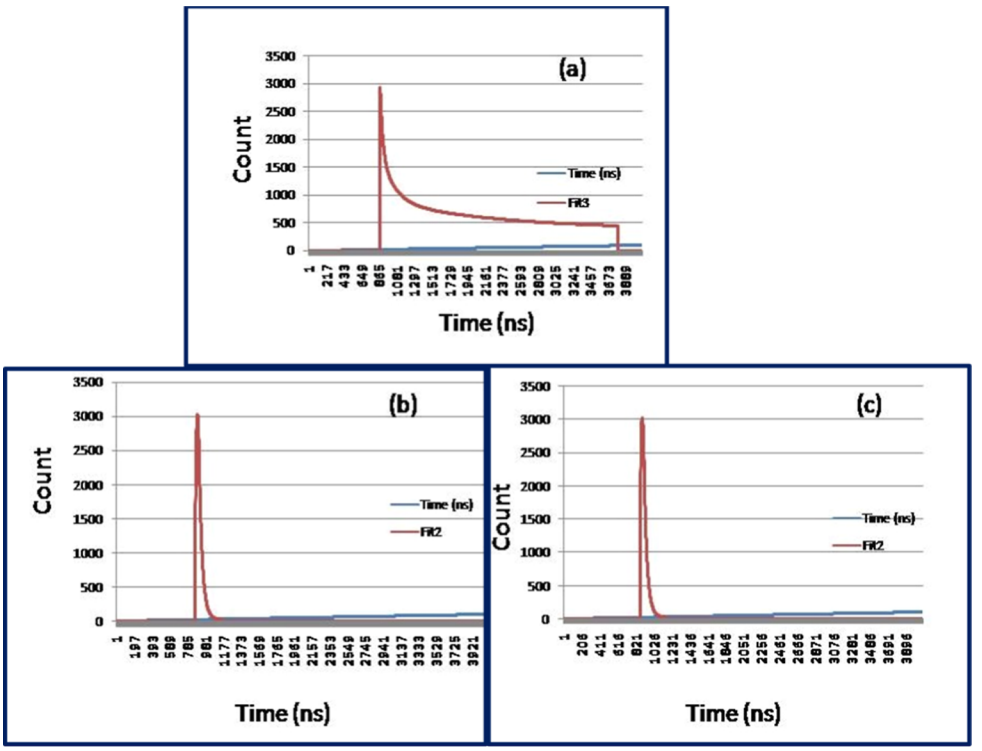

Figure 8. (a–c) Fluorescence decay (TCSPC) of CdS (NRs), $Cd_{0.7}Zn_{0.3}S$ (NRs + NPs), and ZnS NPs.

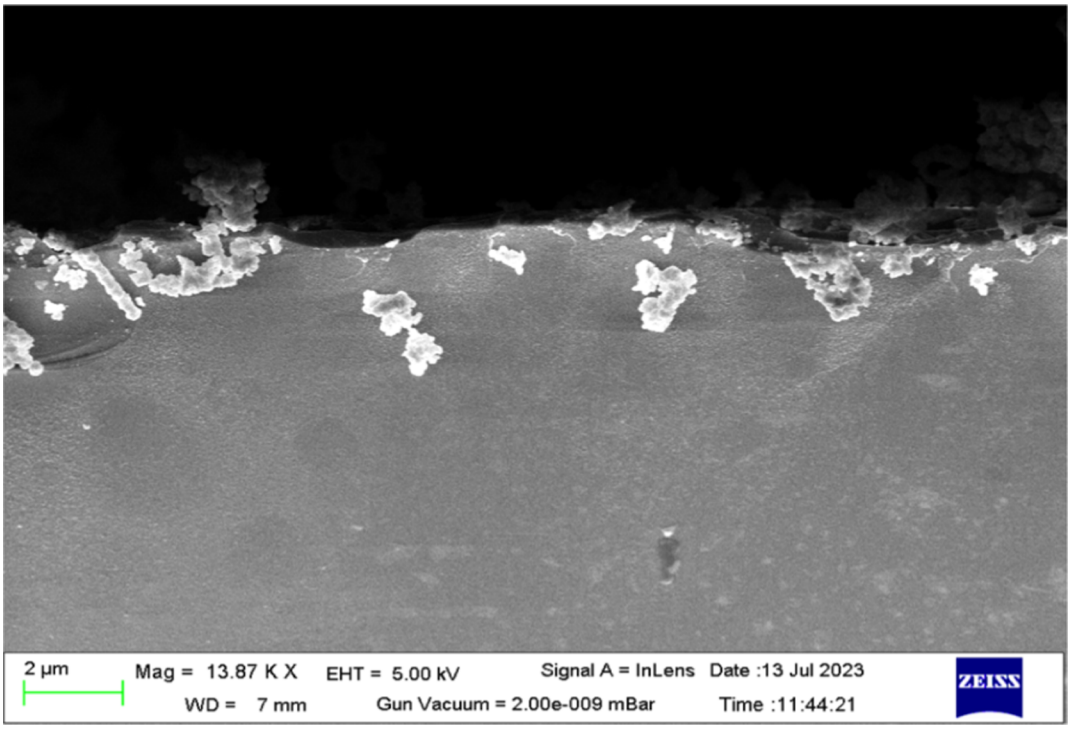

Figure 9. Cross-sectional FESEM of the $Cd_xZn_{1-x}S$ (p)/Si(n) heterojunction device.

images show the predominance of rod shape for CdS and $Cd_{0.7}Zn_{0.3}S$ and spherical shape for ZnS NPS. An optical absorption study indicates the absorption of the peak is due to exciton and the peak shift toward lower wavelength with decrease of "*x*". From the parameters in the table, it is evident that for each material, the band gap is large compared to their bulk values.

Thus, the formation of nanostructures is confirmed, and hence, band gap increases with change of composition as well as with increase of quantum confinement. The Raman study indicates that with an increase of Zn content, the blue shift increases. This means that lattice is more and more strained in $Cd_xZn_{1-x}S$ with increase of Zn content. Hence, strain will be minimum for CdS NRs, while it will be maximum for ZnS NPs.

https://doi.org/10.1021/acsomega.4c06008
ACS Omega 2025, 10, 294−305

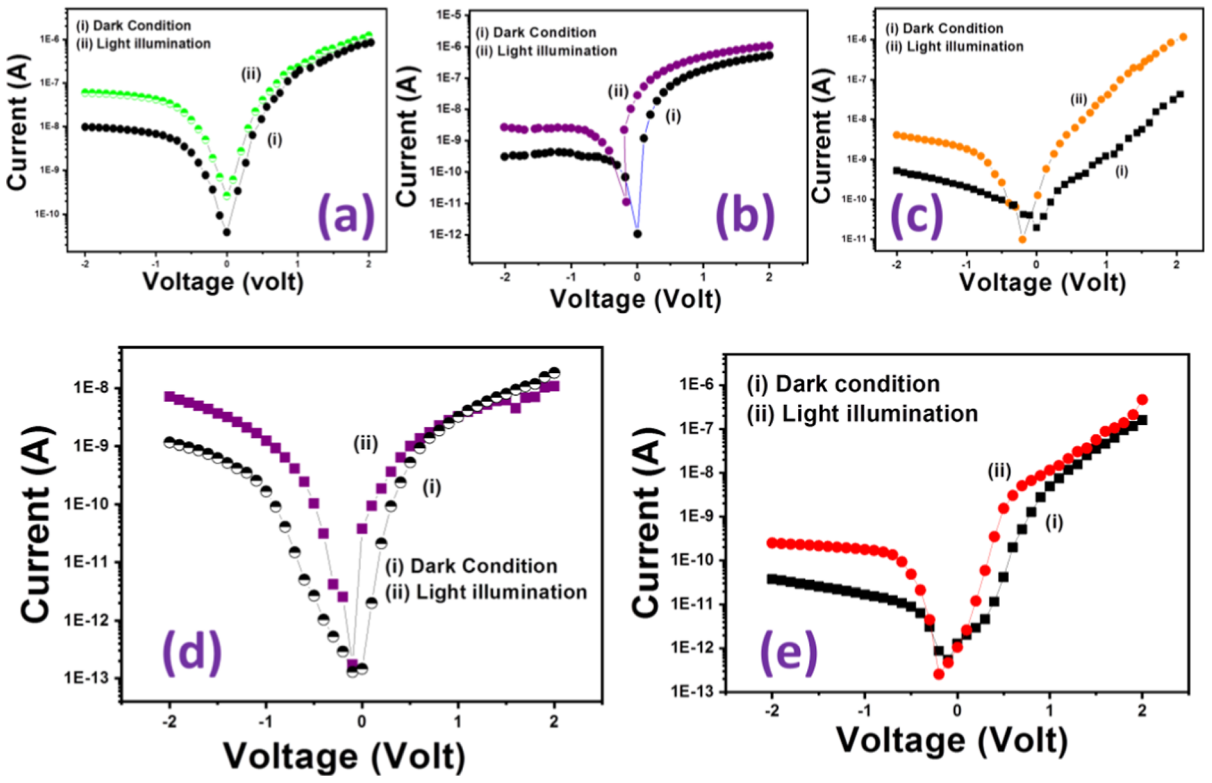

Figure 10. Variation of current (I in Amp.) vs voltage under (a) dark condition and (b) light condition for (a) CdS NRs, (b) $Cd_{0.3}Zn_{0.7}$ NPs, (c) $Cd_{0.5}Zn_{0.5}$ NPs, (d) $Cd_{0.7}Zn_{0.3}$ NPs, and (e) ZnS NPs.

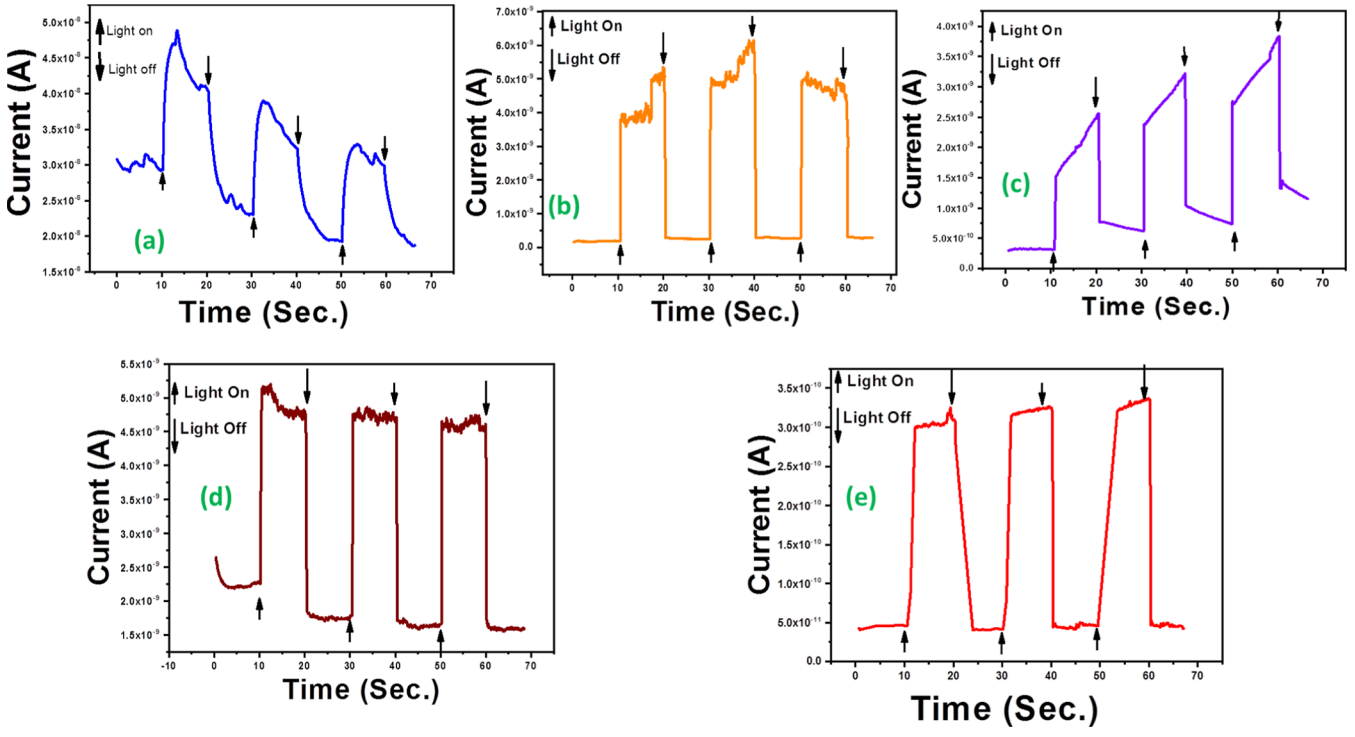

Figure 11. Variation of current (I) vs time under a dark condition (off↓) and light (on↑) condition for (a) CdS NRs, (b) $Cd_{0.7}Zn_{0.3}S$ NPs, (c) $Cd_{0.5}Zn_{0.5}S$ NPs, (d) $Cd_{0.3}Zn_{0.7}S$ NPs, and (e) ZnS NPs.

3.2. Device Analysis. *3.2.1. Current (I)−Voltage (V) Characteristics of the Heterojunction.* Cross-sectional FESEM of the $Cd_xZn_{1-x}S$ (p)/Si(n) heterojunction device is shown in Figure 9. Figure 9 clearly indicates that $Cd_xZn_{1-x}S$ (p) is grown on the n-Si wafer.

The characteristics of the as-fabricated p-$Cd_xZn_{1-x}S$/n-Si heterojunctions are determined from the $I-V$ curves of the heterojunction in dark condition and under visible light illumination and ln(I) vs voltage (V) plots are shown in Figure 10.

https://doi.org/10.1021/acsomega.4c06008
ACS Omega 2025, 10, 294−305

The variation of ln(I) vs voltage (V) within −2 to +2 V under (a) dark condition and (b) illumination with light condition for each fabricated heterojunction based on different compositions is shown in Figure 10.

Responsivity and detectivity of the fabricated heterojunctions are measured from the change of the photocurrent under a reverse bias condition. For a PD, responsivity is a measure of sensitivity to light. It is defined as ratio of photocurrent (Ip_h) to incident light power (P_{opt}) and is defined as

$$R = I_{ph}/P_{opt}\ (\mathrm{A/W}) \tag{8}$$

where I_{ph} = photocurrent density, P_{opt} = optical power density.

The specific detectivity is defined as

$$D^* = A_d^{1/2} R/(eI_{dark})^{1/2} \tag{9}$$

where I_d = dark current, A_d = area of the device.

Responsivity (R) and detectivity (D^*) are determined for each fabricated heterojunction and are shown in Figure 12.

3.2.2. Current (I)−Time (t) Characteristics for Junction Photocurrent Generation under Visible Light Illumination. The current−time variations are shown in Figure 11 for heterojunctions based on nanocrystals of different compositions, i.e., p-$Cd_xZn_{1-x}S$/n-Si. The bias is fixed at −2 V for all heterojunctions. The rise time and fall time are measured using a single pulse for each heterojunction for a −2 V bias condition.

Response time (τ) is the rise time to rise to 90% from 10% of saturation current, while decay time is the time to decay from 90% to 10% of saturation current.

$$\mathrm{Gain} = \tau_{pl}/\tau_{Res} \tag{10}$$

where τ_{pl} = photoluminescence lifetime, τ_{Res} = response time.

The response time is thus an important parameter that determines the performance of a detector.

The time-dependent current (I−t) curves of fabricated PDs with on−off switching are shown in Figure 11 under 100 mw/cm^2 of light and in the dark with a voltage bias of −2 V. For all PDs, the photocurrent of the devices sharply increases to saturation. The current becomes stable after saturation and then a rapid decay of current occurs when the light is switched off. These devices' high on/off ratios shift depending on the composition.

Responsivity and detectivity of the fabricated heterojunction are measured using eqs 8 and 9. Responsivity is maximum for CdS nanorods based heterojunction. However, responsivity decreases gradually for heterojunctions based on other compositions in which Zn content increases (Figure 12).

The present work systematically points that optical parameters like detectivity, responsivity, response time, and gain change with change of compositions $Cd_xZn_{1-x}S$, i.e., with change of band gap in hybrid heterojunctions [$Cd_xZn_{1-x}S$/Si(n)], keeping the intensity of light fixed in each case. Also, the study shows systematically the influence of size (XRD), shape of nanoparticles (FESEM study), and strain (Raman and XRD study) with change of compositions on all such optoelectronic parameters. Thus, present work considers photodetection considering all the compositions instead of a particular composition and correlating with structural parameters. Thus, these engineering nanoscale semiconducting materials have good possibilities in developing photodetectors in the wide wavelength region (from visible to UV region).

3.2.3. Junction Photocurrent Mechanism. The light dependent on−off properties, i.e., switching behavior of current

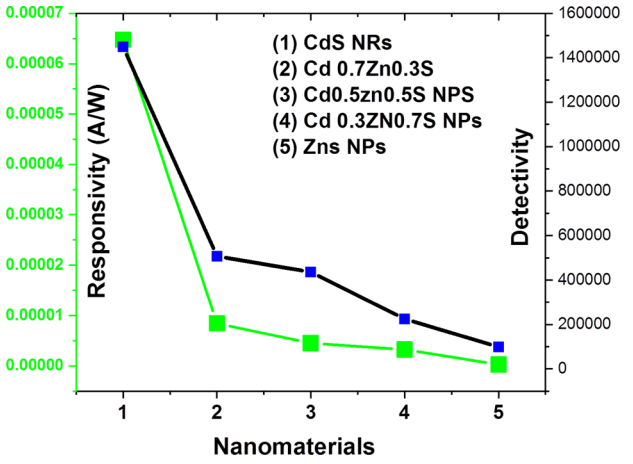

Figure 12. Variation of responsivity and detectivity for p-$Cd_xZn_{1-x}S$/n-Si.

with time indicates that the CdS-based heterojunction converts photon energy to electrical signal more efficiently than devices based on other compositions. This is because the optical absorption coefficient is large for CdS, and this will lead to more photogenerated holes as well as electrons, and it is shown in the band diagram (Figure 13) of p-$Cd_xZn_{1-x}S$/n-Si heterojunction. The energy band diagram can be used to understand that the photocurrent is related to photogenerated carriers in the heterojunction under light irradiation.[18,36] The built-in electric field can direct photogenerated electrons and holes in the space charge region toward the n-Si and p-CdS NRs, respectively, when illuminated. Additionally, from the edge of the space charge zone, photogenerated electron−hole pairs in the p-CdS NRs side can diffuse to the space charge region within one minority carrier diffuse length, where they can then be removed by the built-in electric field.[18] The p-side's photogenerated electrons will therefore move to the n-side. The photogenerated electors and holes will cause a significant change in illumination to current. When p-CdS NRs and n-Si are coupled by a load, both processes produce a photocurrent.

Also, FESEM images indicate the formation of nanorods, which will also enhance the absorption in CdS of incident light compared to other compositions. The band diagram of three typical compositions of p-$Cd_xZn_{1-x}S$/n-Si is shown in Figure 13. The band diagram of three different composition-based heterojunctions indicates the increase of the band gap with a decrease of x in $Cd_xZn_{1-x}S$, whereas the band gap on the Si side remains the same.

The devices [p-$Cd_xZn_{1-x}S$/Si(n)] are heterojunctions between varying p type wide band gap nanostructured semiconductors and fixed low band gap bulk n-type silicon. Thus, with an increase of band gap due to a change of composition of $Cd_xZn_{1-x}S$ (as x varies from 1 to 0), the built-in voltage across the heterojunction also increases due to an increase of separation of Fermi levels of two materials at the junction. Thus, bending of band increases due to change of potential gradient with change of composition. The band bending[37−39] determined from Poisson's equation strongly affects the current−transport mechanism in these heterojunctions. Under constant illumination, the electron−hole pairs will be generated in p-$Cd_xZn_{1-x}S$ as well as in the depletion region and will move out due to the existing field at the junction. The electron−hole pair generation will be less even under same illumination as Zn content increases (i.e., x

https://doi.org/10.1021/acsomega.4c06008
ACS Omega 2025, 10, 294−305

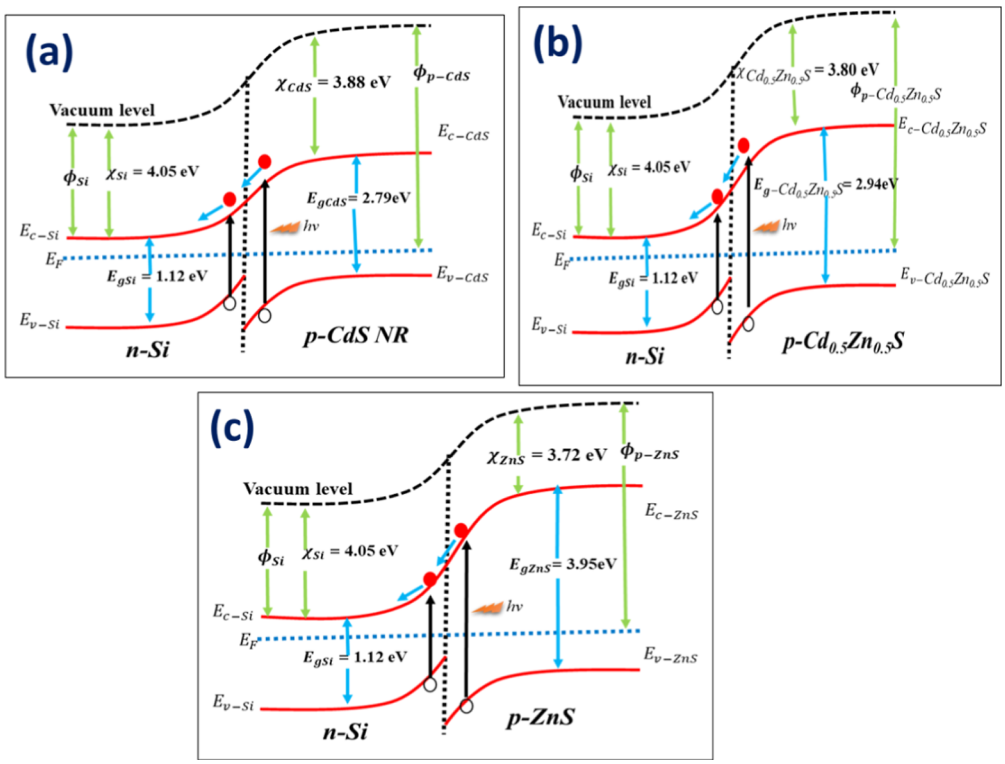

Figure 13. Band diagram of (a) CdS/n-Si, (b) p-$Cd_{0.5}Zn_{0.5}S$/n-Si, and (c) ZnS/n-Si heterojunction.

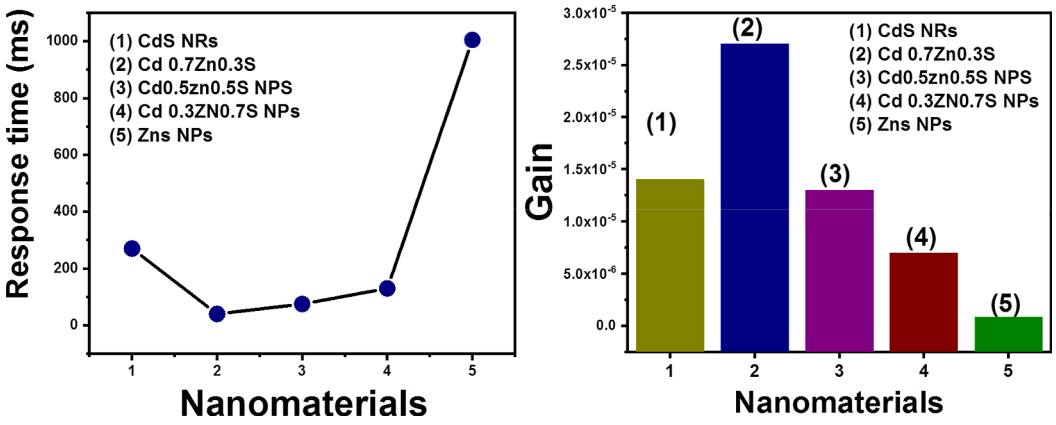

Figure 14. (a) Variation of response time p-$Cd_xZn_{1-x}S$/n-Si heterojunctions and (b) histogram for the variation of the gain vs nanomaterials.

decreases) in p-$Cd_xZn_{1-x}S$. Thus, probability of electron−hole pair generation will be less as band gap increases with increase of Zn in p-$Cd_xZn_{1-x}S$.[40]

Thus, responsivity is 6.474 × 10^{-5} (A/W) for the CdS nanorod-based heterojunction. However, the responsivity decreases gradually for the heterojunction based on other compositions. Hence, responsivity is low, i.e., 2.721 × 10^{-7} (A/W) for ZnS-based heterojunction. The detectivity is 1.45 × 10^6 Jones for CdS-based heterojunction and is large compared to other $Cd_xZn_{1-x}S$-based heterojunctions. This is due to the high absorption coefficient of CdS as well as of its nanorod formation. The significantly increased photoelectric performances of hybrid CdS NRs/Si originate from the microstructural characteristics, which determine the response of photo-induced carriers. With increase of the Zn component in $Cd_xZn_{1-x}S$, the responsivity and the detectivity decrease. Thus, detectivity is as low as 9.83 × 10^4 Jones for ZnS(P)/n-Si. This is because of the increase of band gap with compositional change and more quantum confinement in the transition from CdS to ZnS as well as the shape of nanostructures from nanorods to nanoparticles.

The p-CdS NR/n-Si heterojunction device's photoresponse characteristics were measured at fixed bias (−2 V). The heterojunction's time response to alternating on and off light illumination is shown in Figure 14. It is evident that when light is applied, the electrical current rises sharply and stabilizes at a high-conduction "on" state. When light is removed, however, it rapidly falls to a low-conduction "off" state, resulting in a good I_{light}/I_{dark} ratio with exceptional stability and repeatability. Xie et al. observed a similar phenomenon on CdS nanoribbon/n-Si heterojunctions.[18]

Response time is low for all $Cd_xZn_{1-x}S$ compositions but significantly increases for composition in which x is zero, i.e., for ZnS. response time depends on diffusion time of photo-generated carriers. The Raman study denotes that blue shift

https://doi.org/10.1021/acsomega.4c06008
ACS Omega 2025, 10, 294−305

Table 2. Comparison of Responsivity, Detectivity, Response Time, and Gain Characteristics of Photo Detectors

sample	$I_{d\ (A)}$	$I_{light\ (A)}$	$\Delta I_{ph\ (A)}$	J_{ph} (mA/cm^2)	responsivity (A/W)	detectivity (Jones)	response time (ms)	gain × 10^{-3}
CdS NRs	9.85×10^{-9}	6.07×10^{-8}	5.08×10^{-8}	0.00648	6.474×10^{-6}	1.45×10^{6}	270	0.014
$Cd_{0.7}Zn_{0.3}S$ NRs + NPs	1.36×10^{-9}	8.00×10^{-9}	6.64×10^{-9}	0.00085	8.452×10^{-6}	5.07×10^{5}	40	0.027
$Cd_{0.5}Zn_{0.5}S$ NPs	5.22×10^{-9}	4.05×10^{-9}	3.53×10^{-9}	0.00046	4.493×10^{-6}	4.36×10^{5}	75	0.013
$Cd_{0.3}Zn_{0.7}S$ NPs	3×10^{-10}	2.8×10^{-9}	2.5×10^{-9}	0.000325	3.25×10^{-6}	2.25×10^{5}	130	0.007
ZnS NPs	3.76×10^{-11}	2.51×10^{-10}	2.14×10^{-10}	2.72161×10^{-5}	2.721×10^{-7}	9.8×10^{4}	1005	0 0.0008

increases with increase of Zn content in $Cd_xZn_{1-x}S$. The lattice will be more compressed as the size of the crystal is reduced and in turn increases strain. Pak et al. demonstrated how the bending of energy bands, which impacts photogenerated carrier transport, caused strain-induced barrier modulation to alter photoresponse characteristics in a MoS_2 flexible photodectors.[36] Hence, with an increase of Zn content, the blue shift increases and the response time is found to have a high value of 1005 ms for ZnS NPs. Gain is determined for each photo detector using eq 5. It is evident from Table 2 that the gain is maximum (0.027) for $Cd_{0.7}Zn_{0.3}S$, but it gradually decreases as the Zn content increases in $Cd_xZn_{1-x}S$. This is due to the increase of the response time with an increase of the Zn content. The increase of Zn will introduce more trap as well as recombination center in the forbidden region. As a result, the carriers will be trapped and will be slowly released increasing the response time.

4. CONCLUSIONS

Thus, $Cd_xZn_{1-x}S$ nanomaterials with varying compositions are grown successfully by the chemical reduction route. XRD reveals change of the hexagonal wurtzite phase to cubic zinc blende phase with change of composition. Change of shape is evident from CdS nanorods to ZnS nanoparticles with the increase of Zn content in $Cd_xZn_{1-x}S$ and also leads to the change of band gap. The increase of band gap is also due to quantum confinement. Fluorescence lifetime and Raman shift are two important parameters to explain PD device characteristics of successfully grown nanostructures of $Cd_xZn_{1-x}S$ on Si. Responsivity, detectivity, response time, and gain characteristics of different photo detectors are compared. The result indicates that with decrease of x in $Cd_xZn_{1-x}S$, responsivity, detectivity, and gain decrease, while response time increases. The responsivity and detectivity decrease with increase of Zn content is due to increase of band gap which reduces the absorption possibility in the visible region and also due to the change of shape of nanostructures. The increase of response time is due to the increased strain and also increase of traps introduced by Zn content and hence gain gradually decreases. The quality of the PDs thus degrades as x decreases in $Cd_xZn_{1-x}S$. However, we were able to vary band gap of the composition in a wide range through the variation of x and hence applied these PDs in a wide range of wavelengths.

■ ASSOCIATED CONTENT

Data Availability Statement

Data used are available throughout the manuscript text.

■ AUTHOR INFORMATION

Corresponding Authors

Priyanka Das − *Department of Physics, Vidyasagar University, Paschim, Medinipur 721102, India*;
Email: das.priyanka9733@gmail.com

Satyajit Saha − *Department of Physics, Vidyasagar University, Paschim, Medinipur 721102, India*; orcid.org/0000-0001-5688-6013; Email: sahaphys.vu@gmail.com

Amit Kumar Bhunia − *Department of Physics, Government General Degree College Gopiballavpur-II, Jhargram 721517, India*; orcid.org/0000-0002-7201-1687;
Email: amitphysics87@gmail.com

Complete contact information is available at:
https://pubs.acs.org/10.1021/acsomega.4c06008

Author Contributions

Saha assisted in selecting the topic of the research. S. Saha and A. K. Bhunia supervised completion of this study. After discussing with S. Saha, P. Das prepared the samples, performed the experiments, and collected the data. P. Das analyzed the data by discussing with S. Saha and A. K. Bhunia. All authors read and approved the final manuscript.

Notes

The authors declare no competing financial interest.
This article does not contain any studies involving humans and animals performed by any of the authors.

■ ACKNOWLEDGMENTS

Authors would like to acknowledge MeitY and IIT-Kharagpur for Indian Nanoelectronics Users Program idea to innovation (INUP-i2i). Authors acknowledge the UGC-SAP and DST-FIST sponsored Department of Physics, Vidyasagar University. P.D. acknowledges Higher education, Government of West Bengal, for providing SVMCM scholarship.

■ REFERENCES

(1) Dai, Y.; Wang, X.; Peng, W.; Wu, C.; Ding, Y.; Dong, K.; Wang, Z. L. Enhanced performances of Si/CdS heterojunction near-infrared photodetector by the piezo-phototronic effect. *Nano Energy* **2018**, *44*, 311−318.

(2) Xing, C.; Huang, W.; Xie, Z.; Zhao, J.; Ma, D.; Fan, T.; Liang, W.; Ge, Y.; Dong, B.; Li, J.; Zhang, H. Ultrasmall Bismuth Quantum Dots: facile Liquid-Phase exfoliation, characterization, and application in High-Performance UV−VIS photodetector. *ACS Photonics* **2018**, *5* (2), 621−629.

(3) Li, Z.; Qiao, H.; Guo, Z.; Ren, X.; Huang, Z.; Qi, X.; Dhanabalan, S. C.; Ponraj, J. S.; Zhang, D.; Li, J.; Zhao, J.; Zhong, J.; Zhang, H. High-Performance Photo-Electrochemical Photodetector Based on Liquid-Exfoliated Few-Layered InSe Nanosheets with Enhanced Stability. *Adv. Funct. Mater.* **2018**, *28* (16), 1705237.

(4) Li, S.; Zhang, Y.; Yang, W.; Liu, H.; Fang, X. 2D Perovskite SR2NB3O10 for High-Performance UV Photodetectors. *Adv. Mater.* **2020**, *32* (7), 1905443.

(5) Deng, K.; Li, L. CDS Nanoscale Photodetectors. *Adv. Mater.* **2014**, *26* (17), 2619−2635.

(6) Yang, W.; Hu, K.; Teng, F.; Weng, J.; Zhang, Y.; Fang, X. High-Performance Silicon-Compatible Large-Area UV-to-Visible broadband photodetector based on integrated Lattice-Matched Type II SE/N-SI heterojunctions. *Nano Lett.* **2018**, *18* (8), 4697−4703.

https://doi.org/10.1021/acsomega.4c06008
ACS Omega 2025, 10, 294−305

(7) (a) Cai, S.; Xu, X.; Yang, W.; Chen, J.; Fang, X. Materials and designs for wearable photodetectors. *Adv. Mater.* **2019**, *31* (18), 1808138. (b) Deng, K.; Li, L. CDS Nanoscale Photodetectors. *Adv. Mater.* **2014**, *26* (17), 2619−2635.
(8) Das, P.; Saha, S.; Bhunia, A. K. Visible light dependent degradation of dye: photocatalytic activity of CdS, CdxZn1−xS and ZnS nanoparticles grown by chemical route. *J. Mater. Sci. Mater. Electron.* **2024**, *35* (11), 763.
(9) Flemban, T. H.; Haque, M. A.; Ajia, I.; Alwadai, N.; Mitra, S.; Wu, T.; Roqan, I. S. A Photodetector Based on p-Si/n-ZnO Nanotube Heterojunctions with High Ultraviolet Responsivity. *ACS Appl. Mater. Interfaces* **2017**, *9* (42), 37120−37127.
(10) Alwadai, N.; Haque, M. A.; Mitra, S.; Flemban, T.; Pak, Y.; Wu, T.; Roqan, I. High-Performance Ultraviolet-to-Infrared broadband perovskite photodetectors achieved via Inter-/Intraband transitions. *ACS Appl. Mater. Interfaces* **2017**, *9* (43), 37832−37838.
(11) Velusamy, D. B.; Haque, M. A.; Parida, M. R.; Zhang, F.; Wu, T.; Mohammed, O. F.; Alshareef, H. N. 2D Organic−Inorganic Hybrid thin films for flexible UV−Visible photodetectors. *Adv. Funct. Mater.* **2017**, *27* (15), 1605554.
(12) Yu, X.; Li, Y.; Hu, X.; Zhang, D.; Tao, Y.; Liu, Z.; He, Y.; Haque, M. A.; Liu, Z.; Wu, T.; Wang, Q. J. Narrow bandgap oxide nanoparticles coupled with graphene for high performance mid-infrared photodetection. *Nat. Commun.* **2018**, *9* (1), 4299.
(13) Xu, X.; Li, S.; Chen, J.; Cai, S.; Long, Z.; Fang, X. Design principles and material engineering of ZNS for optoelectronic devices and catalysis. *Adv. Funct. Mater.* **2018**, *28* (36), 1802029.
(14) Tapan, I.; Afrailov, M. A. A ZnS−Si hetero-junction photodiode for short wavelength photon detection. *Nucl. Instrum. Methods Phys. Res., Sect. A* **2003**, *510* (1−2), 92−96.
(15) Liu, J.; Yue, S. Fabrication of ZnS layer on silicon nanopillars surface for photoresistor application. *Chem. Phys. Lett.* **2022**, *801*, 139716.
(16) Ouyang, W.; Teng, F.; He, J.; Fang, X. Enhancing the photoelectric performance of photodetectors based on metal oxide semiconductors by Charge-Carrier Engineering. *Adv. Funct. Mater.* **2019**, *29* (9), 1807672.
(17) Flemban, T. H.; Haque, M. A.; Ajia, I.; Alwadai, N.; Mitra, S.; Wu, T.; Roqan, I. S. A Photodetector Based on p-Si/n-ZnO Nanotube Heterojunctions with High Ultraviolet Responsivity. *ACS Appl. Mater. Interfaces* **2017**, *9* (42), 37120−37127.
(18) Xie, C.; Li, F.; Zeng, L.; Luo, L.; Wang, L.; Wu, C.; Jie, J. Surface charge transfer induced p-CdS nanoribbon/n-Si heterojunctions as fast-speed self-driven photodetectors. *J. Mater. Chem. C* **2015**, *3* (24), 6307−6313.
(19) Alwadai, N.; Haque, M. A.; Mitra, S.; Flemban, T.; Pak, Y.; Wu, T.; Roqan, I. High-Performance Ultraviolet-to-Infrared broadband perovskite photodetectors achieved via Inter-/Intraband transitions. *ACS Appl. Mater. Interfaces* **2017**, *9* (43), 37832−37838.
(20) Ray, S. K.; Mukherjee, S.; Dey, T.; Jana, S.; Koren, E. Two-Dimensional Material-Based quantum dots for Wavelength-Selective, tunable, and broadband photodetector devices. In *Quantum Dot Photodetectors. Lecture Notes in Nanoscale Science and Technology*; Springer, 2021; pp 249−287.
(21) Yu, X.; Li, Y.; Hu, X.; Zhang, D.; Tao, Y.; Liu, Z.; He, Y.; Haque, M. A.; Liu, Z.; Wu, T.; Wang, Q. J. Narrow bandgap oxide nanoparticles coupled with graphene for high performance mid-infrared photodetection. *Nat. Commun.* **2018**, *9* (1), 4299.
(22) Li, L.; Wu, P.; Fang, X.; Zhai, T.; Dai, L.; Liao, M.; Koide, Y.; Wang, H.; Bando, Y.; Golberg, D. Single-Crystalline CDS nanobelts for excellent Field-Emitters and ultrahigh Quantum-Efficiency photodetectors. *Adv. Mater.* **2010**, *22* (29), 3161−3165.
(23) Heo, K.; Lee, H.; Park, Y.; Park, J.; Lim, H.-J.; Yoon, D.; Lee, C.; Kim, M.; Cheong, H.; Park, J.; Jian, J.; Hong, S. Aligned networks of cadmium sulfidenanowires for highly flexible photodetectors with improved photoconductive responses. *J. Mater. Chem.* **2012**, *22* (5), 2173−2179.
(24) Pei, Y.; Pei, R.; Liang, X.; Wang, Y.; Liu, L.; Chen, H.; Liang, J. CdS-Nanowires Flexible Photo-detector with Ag-Nanowires Electrode Based on Non-transfer Process. *Sci. Rep.* **2016**, *6* (1), 21551.
(25) An, Q.; Meng, X.; Sun, P. High-Performance Fully Nanostructured Photodetector with Single-Crystalline CdS Nanotubes as Active Layer and Very Long Ag Nanowires as Transparent Electrodes. *ACS Appl. Mater. Interfaces* **2015**, *7* (41), 22941−22952.
(26) Jin, B.; Huang, P.; Zhang, Q.; Zhou, X.; Zhang, X.; Li, L.; Su, J.; Li, H.; Zhai, T. Self-Limited epitaxial growth of ultrathin nonlayered CDS flakes for High-Performance photodetectors. *Adv. Funct. Mater.* **2018**, *28* (20), 1800181.
(27) Mezzetti, A.; Balandeh, M.; Luo, J.; Bellani, S.; Tacca, A.; Divitini, G.; Cheng, C.; Ducati, C.; Meda, L.; Fan, H.; Di Fonzo, F. Hyperbranched TiO2−CdS nano-heterostructures for highly efficient photoelectrochemical photoanodes. *Nanotechnology* **2018**, *29* (33), 335404.
(28) Luo, M.; Liu, Y.; Hu, J.; Liu, H.; Li, J. One-Pot Synthesis of CdS and Ni-Doped CdS Hollow Spheres with Enhanced Photocatalytic Activity and Durability. *ACS Appl. Mater. Interfaces* **2012**, *4* (3), 1813−1821.
(29) Liu, Y.; Kathan, K.; Saad, W.; Prud'homme, R. K. Ostwald Ripening ofB-Carotene nanoparticles. *Phys. Rev. Lett.* **2007**, *98* (3), 036102.
(30) Hassan, Md. S.; Bera, S.; Gupta, D.; Ray, S. K.; Sapra, S. MoSe2−Cu2S Vertical p−n Nanoheterostructures for High-Performance Photodetectors. *ACS Appl. Mater. Interfaces* **2019**, *11* (4), 4074−4083.
(31) Silambarasan, K.; Vinoth, E.; Harish, S.; Navaneethan, M.; Hara, K. High spectral responsivity and specific detectivity of p-MoS2/n-Si heterojunction photodetector for near-IR detection via facile solution process. *J. Mater. Sci. Mater. Electron.* **2023**, *34* (28), 1975.
(32) Bhunia, A. K.; Ghosh, T. N.; Bhunia, K.; Saha, S. Nonlinear alternating current conduction study in manganese-doped zinc oxide nanocapsules and nanoplates. *Appl. Phys. A: Mater. Sci. Process.* **2023**, *129* (2), 81.
(33) Kumar, P.; Saxena, N.; Chandra, R.; Gupta, V.; Agarwal, A.; Kanjilal, D. Nanotwinning and structural phase transition in CdS quantum dots. *Nanoscale Res. Lett.* **2012**, *7* (1), 584.
(34) Vasiljevic, Z. Z.; Dojcinovic, M. P.; Vujancevic, J. D.; Jankovic-Castvan, I.; Ognjanovic, M.; Tadic, N. B.; Stojadinovic, S.; Brankovic, G. O.; Nikolic, M. V. Photocatalytic degradation of methylene blue under natural sunlight using iron titanate nanoparticles prepared by a modified sol−gel method. *R. Soc. Open Sci.* **2020**, *7* (9), 200708.
(35) Liu, Y.; Kathan, K.; Saad, W.; Prud'homme, R. K. Ostwald Ripening ofB-Carotene nanoparticles. *Phys. Rev. Lett.* **2007**, *98* (3), 036102.
(36) Pak, S.; Lee, J.; Jang, A.; Kim, S.; Park, K.; Sohn, J. I.; Cha, S. Strain-Engineering of contact energy barriers and photoresponse behaviors in monolayer MOS_2 flexible devices. *Adv. Funct. Mater.* **2020**, *30* (43), 2002023.
(37) Guidara, M. A.; Bouaziz, M. A.; Schmitt, C.; Azari, Z.; Hadj-Taieb, E. A semi-empirical model for structural integrity assessment of defected high density polyethylene pipes. *Eng. Fail. Anal.* **2019**, *100*, 273−287.
(38) Sze, S. M. *Physics of Semiconductor Devices*, 2nd ed.; Wiley: New York, 1981; Chapters 1 and 2.
(39) Mouthaan, T. *Semiconductor Devices Explained Using Active Simulation*; Wiley: New York, 1999; Chapters 1 and 2.
(40) Matsuura, H. Calculation of band bending in ferroelectric semiconductor. *New J. Phys.* **2000**, *2*, 8.

https://doi.org/10.1021/acsomega.4c06008
ACS Omega 2025, 10, 294−305